

Dynamics of the Desai-Zwanzig model in multi-well and random energy landscapes

Susana N. Gomes *

Serafim Kalliadasis †

Grigorios A. Pavliotis ‡

Petr Yatsyshin §

February 7, 2019

Abstract

We analyze a variant of the Desai-Zwanzig model [J. Stat. Phys. **19** 1-24 (1978)]. In particular, we study stationary states of the mean field limit for a system of weakly interacting diffusions moving in a multi-well potential energy landscape, coupled via a Curie-Weiss type (quadratic) interaction potential. The location and depth of the local minima of the potential are either deterministic or random. We characterize the structure and nature of bifurcations and phase transitions for this system, by means of extensive numerical simulations and of analytical calculations for an explicitly solvable model. Our numerical experiments are based on Monte Carlo simulations, the numerical solution of the time-dependent nonlinear Fokker-Planck (McKean-Vlasov equation), the minimization of the free energy functional and a continuation algorithm for the stationary solutions.

1 Introduction

Systems of interacting particles, often subject to thermal noise, arise in a wide spectrum of natural phenomena and applications, ranging from plasma physics and galactic dynamics [6] to dynamical density-functional theory (DDFT) [25, 23], mathematical biology [18, 31] and even in mathematical models in social sciences [21, 35]. As examples of models of interacting “agents” in a noisy environment that appear in the social sciences, including crowd dynamics, we mention the modeling of cooperative behavior [13], risk management [20] and opinion formation [21]. Other recent applications that have motivated this work are global optimization [40], active media [3] and machine learning. Indeed, it has been shown recently [41, 43] that “stochastic gradient descent”, the optimization algorithm used in the training of neural networks, can be represented as the evolution of a particle system with interactions governed by a potential related to the objective function that is used to train the network. Several of the issues that we study here, such as phase transitions and the effect of nonconvexity, are of great interest in the context of the training of neural networks.

For weakly interacting diffusions, one can pass rigorously to the mean-field limit leading to the McKean-Vlasov equation, a nonlinear nonlocal Fokker-Planck type Eq. [33, 13]. Unlike finite systems of interacting diffusions, whose law (probability density function) is governed by the

*Mathematics Institute, University of Warwick (susana.gomes@warwick.ac.uk)

†Department of Chemical Engineering, Imperial College London

‡Department of Mathematics, Imperial College London

§Department of Chemical Engineering, Imperial College London

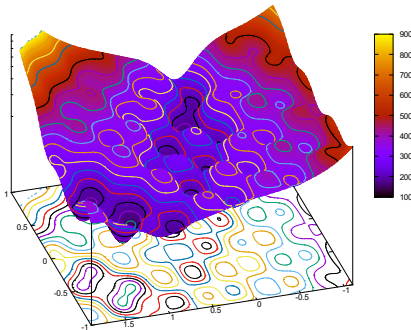


Figure 1: A 2D multiscale potential.

linear Fokker-Planck equation, the McKean-Vlasov equation can exhibit phase transitions [13]. Indeed, whereas a finite system of interacting overdamped Langevin diffusions moving in a confining potential is always ergodic with respect to the Gibbs measure [38, Ch. 4], the McKean-Vlasov equation with a non-convex confining potential, can have several stationary solutions at low temperatures [13, 44]. As a matter of fact, the number of stationary solutions depends on the number of metastable states (local minima) of the confining potential [45]. A complete rigorous analysis of phase transitions, both continuous and discontinuous, for the McKean-Vlasov dynamics in a box with periodic boundary conditions and for non-convex (i.e. non-H stable) interaction potentials is presented in [10]. The mean field limit for non-Markovian interacting particles, including the effect of memory on the bifurcation diagram, is studied in [17].

The main purpose of this study is to scrutinize the dynamics of a system of weakly interacting diffusions and, in particular, characterize bifurcations and phase transitions for this system in the presence of a multi-well confining potential which can have random locations and depths of local minima, interacting under a quadratic Curie-Weiss potential. An example of a deterministic multi-well potential is given in Fig. 1. It is a modified version of the so-called Müller-Brown potential [36], a canonical potential surface used often as a prototype in theoretical chemistry including reaction dynamics [27], but also theoretical biology including protein folding [12]. The potential is also often adopted as a prototype to test the performance of computational optimization algorithms to e.g. obtain reaction paths [8]. Multi-well potentials/rugged energy landscapes have numerous applications, from materials science and catalysis where (surface) diffusion in a multiscale potential is critical to understanding how atoms or molecules adsorb on catalytic surfaces and react, to droplet motion on chemically heterogeneous substrates [28]. Our study builds upon earlier work [26]. There, the mean field limit for interacting diffusions in a two-scale, locally periodic potential was considered. This problem was then studied using tools from multiscale analysis, and in particular periodic homogenization for parabolic PDEs [39]. In contrast, here the focus is on multi-well potentials (either deterministic or random) that do not have a periodic structure, and, consequently, the theory of periodic homogenization is not applicable.

In particular, we will offer a complete bifurcation analysis and explicit characterization of phase transitions for the McKean-Vlasov equation in one dimension for model multi-well potentials with

an arbitrary number of local minima. And we will also study phase transitions when the number of local minima tends to infinity.

Our starting point is a system of interacting particles in one dimension, moving in a confining potential, $V(\cdot)$, and which interact through an interaction potential $W(\cdot)$ which we consider to be of a quadratic Curie-Weiss type (i.e., $W(x) = \frac{x^2}{2}$):

$$dX_t^i = \left(-V'(X_t^i) - \frac{\theta}{N} \sum_{j=1}^N (X_t^i - X_t^j) \right) dt + \sqrt{2\beta^{-1}} dB_t^i, \quad (1)$$

for $i = 1, \dots, N$. Here $\{X_t^i\}_{i=1}^N$ denotes the position of the interacting agents, θ the strength of the interaction between the agents, $\{B_t^i\}_{i=1}^N$ standard independent one-dimensional Brownian motions and β denotes the inverse temperature. The total energy (Hamiltonian) of the system of interacting diffusions (1) is

$$W_N(\mathbf{X}) = \sum_{\ell=1}^N V(X^\ell) + \frac{\theta}{4N} \sum_{n=1}^N \sum_{\ell=1}^N (X^n - X^\ell)^2, \quad (2)$$

where $\mathbf{X} = (X^1, \dots, X^N)$.

Passing rigorously to the mean field limit as $N \rightarrow \infty$ using, for example, martingale techniques [13, 22, 37], and under appropriate assumptions on the confining potential and on the initial conditions (propagation of chaos), is a well-studied problem. Formally, using the law of large numbers we deduce that

$$\lim_{N \rightarrow +\infty} \frac{1}{N} \sum_{j=1}^N X_t^j = \mathbb{E}X_t,$$

where the expectation is taken with respect to the “1-particle” distribution function $p(x, t)$ – This corresponds to the mean field ansatz for the N -particle distribution function, $p_N(x_1, \dots, x_N, t) = \prod_{n=1}^N p(x_n, t)$ and taking the limit as $N \rightarrow \infty$; see [32, 4]. – Passing, formally, to the limit as $N \rightarrow \infty$ in the stochastic differential equation (1), we obtain the McKean stochastic differential equation (SDE)

$$dX_t = -V'(X_t) dt - \theta(X_t - \mathbb{E}X_t) dt + \sqrt{2\beta^{-1}} dB_t. \quad (3)$$

The Fokker-Planck equation corresponding to this SDE is the McKean-Vlasov equation [19, 34, 33]

$$\frac{\partial p}{\partial t} = \frac{\partial}{\partial x} \left(V'(x)p + \theta (W' \star p) p + \beta^{-1} \frac{\partial p}{\partial x} \right), \quad (4)$$

where \star denotes the convolution operator. The McKean-Vlasov equation is a nonlinear, nonlocal equation, sometimes referred to as the McKean-Vlasov-Fokker-Planck equation. It is a gradient flow, with respect to the Wasserstein metric, for the free energy functional

$$\mathcal{F}[\rho] = \beta^{-1} \int \rho \ln \rho dx + \int V \rho dx + \frac{\theta}{2} \iint W(x-y) \rho(x) \rho(y) dx dy. \quad (5)$$

Background material on the McKean-Vlasov equation can be found in, e.g. [19, 11, 46]. The equation belongs to the broad class of (entropic) gradient flows. Various technical questions, such as the connection between gradient flows and large deviations are addressed in [15, 1].

It is noteworthy that the system of interacting Langevin equations (1) as well as the potential energy (2) retain the basic features of the models studied in DDFT for classical fluids [25, 23].

One approach used to derive DDFT is to start with the Langevin dynamics of Brownian particles to obtain a Fokker-Planck equation for the n -particle probability distribution. A formal BBGKY hierarchy then is used to obtain a closed equation for the density distribution. The main assumption is an equilibrium thermodynamic sum rule, the so-called adiabatic approximation, by which the higher-body correlations are approximated by those of an equilibrium fluid with the same density distribution. Including hydrodynamic interactions in DDFT to obtain a hydrodynamic description that includes intermolecular interactions is non-trivial [23, 24].

On the other hand, the Vlasov equation, originally derived for ionized gases, i.e. plasma with long-range (Coulomb) forces, describing the time evolution of the distribution function of plasma, is somewhere halfway between an n -particle model and the hydrodynamic description. The latter can be rigorously obtained starting from the Langevin dynamics assuming there is no bath, replace the potential with the Boltzmann collision operator to get the Boltzmann equation, and then use homogenization (as in [25]). But the standard kinetic approach based on the Boltzmann equation cannot be applied for Coulomb forces which are long range and cannot be treated as collisions (unless a gas is weakly ionized, in which case the charge-charge interactions are negligible with respect to collisions with neutrals). Instead, one has to start with the collisionless Boltzmann equation and appropriately adapt it to plasma by also utilizing Maxwell's equations (but in most cases of practical interest that time variations of the fields in the Maxwell's equations are negligible) and the quasi-static fields are considered instead.

The finite dimensional dynamics (1) has a unique invariant measure. Indeed, the process \mathbf{X}_t defined in (1) is always ergodic, and in fact reversible, with respect to the Gibbs measure [38, Ch. 4],

$$\mu_N(dx) = \frac{1}{Z_N} e^{-\beta W_N(x^1, \dots, x^N)} dx^1 \dots dx^N, \quad (6a)$$

$$Z_N = \int_{\mathbb{R}^N} e^{-\beta W_N(x^1, \dots, x^N)} dx^1 \dots dx^N \quad (6b)$$

where $W_N(\cdot)$ is given by (2). On the other hand, the McKean dynamics (3) and the corresponding McKean-Vlasov-Fokker-Planck equation (4) can have more than one invariant measures, for non-convex confining potentials and at sufficiently low temperatures [13, 44]. This is not surprising, since the McKean-Vlasov equation is a nonlinear, nonlocal PDE, as already noted, and the standard uniqueness of solutions for the linear (stationary) Fokker-Planck equation does not apply [7].

The density of the invariant measure(s) for the McKean dynamics (3) satisfies the stationary nonlinear Fokker-Planck equation

$$\frac{\partial}{\partial x} \left(V'(x)p_\infty + \theta (W' \star p) p_\infty + \beta^{-1} \frac{\partial p_\infty}{\partial x} \right) = 0. \quad (7)$$

Based on earlier work [13, 44], it is by now well understood that the number of invariant measures, i.e. the number of solutions to (7), is related to the number of metastable states (local minima) of the confining potential – see [45] and the references therein.

For the Curie-Weiss (i.e. quadratic) interaction potential, we can write Eq. (4) as a Fokker-Planck equation with a dynamic constraint

$$\frac{\partial p}{\partial t} = \beta^{-1} \frac{\partial^2 p}{\partial x^2} + \frac{\partial}{\partial x} (V'(x)p - \theta(m - x)p), \quad (8)$$

$$m = R(m) = \int_{\mathbb{R}} xp(x, t) dx, \quad (9)$$

and, from the corresponding steady-state equation, a one-parameter family of solutions to the stationary McKean-Vlasov equation (7) can be obtained:

$$p_\infty(x; \theta, \beta, m) = \frac{1}{Z(\theta, \beta; m)} e^{-\beta(V(x) + \theta(\frac{1}{2}x^2 - xm))}, \quad (10a)$$

$$Z(\theta, \beta; m) = \int_{\mathbb{R}} e^{-\beta(V(x) + \theta(\frac{1}{2}x^2 - xm))} dx. \quad (10b)$$

This one-parameter family of probability densities is subject, of course, to the constraint that it provides us with the correct formula for the first moment:

$$m = \int_{\mathbb{R}} xp_\infty(x; \theta, \beta, m) dx =: R(m; \theta, \beta). \quad (11)$$

We will refer to this as the **selfconsistency** equation and it will be the main object of study of this paper. Once a solution to (11) has been obtained, substitution back into (10) yields a formula for the invariant density $p_\infty(x; \theta, \beta, m)$.

Clearly, the number of invariant measures of the McKean-Vlasov dynamics is determined by the number of solutions to the selfconsistency equation (11). It is well known and not difficult to prove that for symmetric nonconvex confining potentials a unique invariant measure exists at sufficiently high temperatures, whereas more than one invariant measures exist below a critical temperature β_c^{-1} [13, Thm. 3.3.2], [44, Thm. 4.1, Thm. 4.2], see also [42]. In particular, for symmetric potentials, $m = 0$ is always a solution to the selfconsistency equation (11). Above β_c , i.e. at sufficiently low temperatures, the zero solution loses stability and a new branch bifurcates from the $m = 0$ solution [42]. This second-order phase transition is similar to the one familiar from the theory of magnetization and the study of the Ising model. It will become clear later on this study that for multi-well potentials the value of θ also plays a role on the type of bifurcations obtained and therefore it is important to keep both parameters in our analysis.

Another important property of the solutions of the Fokker-Planck equation (4) is the critical temperature β_C at which pitchfork bifurcations from the mean zero solution occur. This critical temperature is a function of θ , and is given [42] by the solution to the equation

$$\text{Var}(m = 0, \theta, \beta) := \int x^2 p_\infty(x; m = 0, \theta, \beta) dx = \beta^{-1} \theta^{-1}. \quad (12)$$

This equation can be solved numerically for the potentials we will study in this paper.

The structure and number of equilibrium states for the generalized Desai-Zwanzing model that we consider can be studied using four different approaches:

1. As the invariant measure(s) of the particle dynamics (1), in the limit as the number of particles becomes infinite.
2. As the long time limit of solutions to the time-dependent nonlinear Fokker-Planck equation (4).
3. As minimizers of the free energy functional (5).
4. In terms of solutions to the self-consistency equation (11).

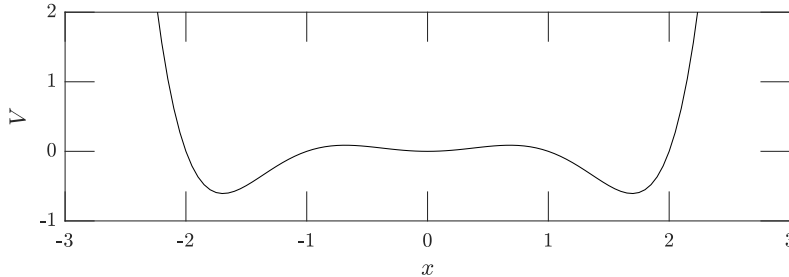


Figure 2: A polynomial potential of the form (13), where $M = 3$.

We will use all of these in order to construct the bifurcation diagrams for the stationary states of (4).

The rest of the paper is organized as follows. In Section 2 we briefly summarize the models (i.e., the types of confining potentials) we consider in our study, and present the different methodologies we will use to construct the bifurcation diagrams and analyze the stability of each branch. In Section 3 we present extensive numerical experiments we performed to obtain the bifurcation diagram for different types of potentials, including calculations of the free-energy surfaces associated with each system, of the bifurcation diagrams of the first moment m as a function of the inverse temperature β and of the critical temperature β_C as a function of θ as well as time-dependent simulations of the particle system and the corresponding McKean-Vlasov equation. A discussion and conclusions are offered in Section 4.

2 Models studied and methodology

In this section we outline the model confining potentials that we will consider and we also provide details of the mathematical and computational techniques that we will use.

2.1 Models studied in this paper

Consider the system of weakly interacting diffusions given in (1). As already emphasized, the interaction is taken to be of the Curie-Weiss type ($W(x) = \frac{x^2}{2}$) and different types of confining multi-well potentials will be considered. In particular, we will study the following potentials.

1. Polynomial potentials of the form (see, e.g., Fig. 2)

$$V(x) = \sum_{\ell=1}^M a_{\ell} x^{2\ell}. \quad (13)$$

2. Rational potentials ([51]) with an arbitrary number of local minima and with (possibly) random location and depths of local minima, see, e.g., Fig. 3.

$$V(x) = \frac{1}{\sum_{\ell=-M}^M \delta_{\ell} |x - c_{\ell} x_{\ell}|^{-2}}, \quad (14)$$

where we consider both deterministic and random distributions of $\{\delta_{\ell}, c_{\ell}\}$ and where in the random case we take these distributions to be uniform.

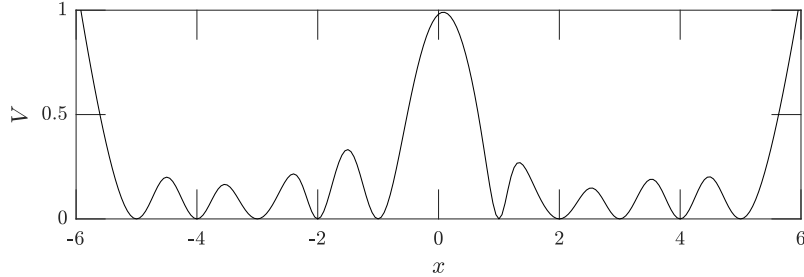


Figure 3: A realization of a potential of the form (14) with 10 local minima located at the integers between -5 and 5 ($c_\ell = 1$) and separated by arbitrary heights ($\delta_\ell \sim U([0, 1])$).

3. Piecewise linear potentials with quadratic growth at infinity,

$$V(x) = \begin{cases} \frac{x^2 - x_M^2}{2}, & \text{if } |x| \geq x_M, \\ \frac{(H_i - h_i)x}{x_{i+\frac{1}{2}} - x_i} + \frac{h_i x_{i+\frac{1}{2}} - H_i x_i}{x_{i+\frac{1}{2}} - x_i}, & \text{if } x_i < x < x_{i+\frac{1}{2}}, \\ \frac{(h_i - H_i)x}{x_{i+1} - x_{i+\frac{1}{2}}} + \frac{H_i x_{i+1} - h_i x_{i+\frac{1}{2}}}{x_{i+1} - x_{i+\frac{1}{2}}}, & \text{if } x_{i+\frac{1}{2}} < x < x_{i+1}. \end{cases} \quad (15)$$

2.2 Methodology

Our aim is to study the bifurcation diagram of the invariant measures of the system of SDEs (1). We will do that by considering the mean-field limit of this system, given by Eq. (3). In this limit, the density of the particles satisfies the nonlinear nonlocal Fokker-Planck equation (4). The invariant measure(s) of the system (1) satisfy the stationary Fokker-Planck equation (7). Depending on the interaction potential, and the parameters θ and β , there will exist only one (for sufficiently small beta) or multiple (for large β) solutions. The number of these solutions depends on the number of local minima and maxima of the confining potential V .

We construct the bifurcation diagram using the first moment $m = m_1 = \mathbb{E}(X_t)$ as the order parameter and plot it as a function of the inverse temperature β for a fixed value of θ . We will use two methods to obtain the bifurcation diagram:

1. Using the fact that equilibrium states are minimizers of the free-energy functional (5). We can then find the equilibrium points using differential geometry techniques. This methodology has the advantage that it immediately gives us the stability of each branch - stable solutions are local minima of the free-energy, while its local maxima are unstable solutions.
2. Arclength continuation to solve the self-consistency equation (11). For the case of polynomial potentials, we can also use this technique to solve a system of ordinary differential equations (ODEs) for the moments (details are given in section 3.1). Our continuation scheme makes use of a modification of MATLAB's `matcont` routine (details are given in section 2.2.2).

Both methods have been used successfully in our previous studies to perform detailed parametric studies and compute adsorption isotherms, bifurcations of equilibrium states, phase diagrams and critical points for fluids in confinement using DFT (e.g. [47, 48, 49, 50]).

Our results are confirmed by performing a careful comparison of the bifurcation diagrams obtained with the long-time behavior of solutions to the Fokker-Planck equation, as well as Monte-Carlo (MC) simulations of the corresponding particle system.

2.2.1 Free-energy formulation

We make use the fact that the stationary solutions of the Fokker-Planck equation (4) are equilibrium points of the free energy given by Eq. (5). In particular, since we know the form of the steady solutions $p_\infty(m; \theta, \beta)$, we can compute the free-energy surface as a function of the two arguments, m and β , for a fixed value of θ , $\mathcal{F}(m, \beta; \theta)$. By computing its equilibrium points, we can then plot the desired bifurcation diagram. This methodology also allows us to immediately evaluate the stability of each branch, since local minima correspond to stable solutions, while local maxima are unstable ones. The bifurcation diagrams obtained with this method suffer from poor resolution near branching points. However, the resolution at higher values of β allows us to easily find initial guesses for the arclength continuation process which we describe below, and also guarantees that we have information about all the existing branches.

A useful observation which we will make use of is that the free energy of the equilibrium states can be calculated in a quite explicit form which depends only on the partition function and on the mean:

Proposition 2.1. *The free energy of an equilibrium state (10)-(11) is given by*

$$\mathcal{F}[p] = -\beta^{-1} \log Z + \frac{\theta}{2} m^2.$$

In particular, when $m = 0$ we have

$$\mathcal{F}[p] = -\beta^{-1} \log Z.$$

Proof. The free energy of a function p is given by

$$\mathcal{F}[p] = \beta^{-1} \int_{\mathbb{R}} p(x) \log(p(x)) dx + \int_{\mathbb{R}} V(x) p(x) dx + \frac{\theta}{2} \int_{\mathbb{R}} \int_{\mathbb{R}} W(x-y) p(x) p(y) dx dy.$$

The stationary solution(s) to the Fokker-Planck equation (4) are given by Eqs. (10)-(11). Plugging this into the expression for the free energy, we obtain

$$\mathcal{F}[p] = \beta^{-1} \int_{\mathbb{R}} p(x) (-\beta (V(x) + \theta(W \star p)) - \log Z) dx + \int_{\mathbb{R}} V(x) p(x) dx + \quad (16)$$

$$+ \frac{\theta}{2} \int_{\mathbb{R}} \int_{\mathbb{R}} W(x-y) p(x) p(y) dx dy$$

$$= -\beta^{-1} \log Z - \frac{\theta}{2} \int_{\mathbb{R}} \int_{\mathbb{R}} W(x-y) p(x) p(y) dx dy, \quad (17)$$

where we have used that $\int_{\mathbb{R}} p(x) dx = 1$ and the definition of convolution.

Replacing $W(x-y) = \frac{(x-y)^2}{2}$ and using Eq. (10), yields

$$\mathcal{F}[p] = -\beta^{-1} \log Z + \theta R(m) \left(m - \frac{1}{2} R(m) \right). \quad (18)$$

We note that when p is an equilibrium solution of the Fokker-Planck equation, then $R(m) = m$ and we obtain

$$\mathcal{F}[p] = -\beta^{-1} \log Z + \frac{\theta}{2} m^2,$$

and, when $m = 0$ we recover

$$\mathcal{F}[p] = -\beta^{-1} \log Z.$$

□

2.2.2 Arclength continuation

The second method we use is arclength continuation of solutions, for which we will use the Moore-Penrose quasi arclength continuation algorithm. Rigorous mathematical construction of the full arclength continuation methodology can be found in [29, 2]. Some useful practical aspects of implementing arclength continuation are also given in the MATLAB manual [14]. The idea is to solve the discretized nonlinear algebraic equation (10)-(11) for a given initial value of the control parameter, β_0 , and a given initial guess, m_0 , relaxing the dependence on β_0 and adding a condition of curve continuity in the phase space of solutions to the discretized problem. The method then provides us with a way of following each branch by computing tangent vectors.

We use arclength continuation to construct the bifurcation diagram of steady solutions of (4) using the self-consistency equation (11) and the system of equations for the moments described in the next section. Arclength continuation is also used to solve the equation for the critical temperature β_C given by the solution of (12) as a function of θ .

2.2.3 Time dependent simulations

To simulate the corresponding particle system, we perform MC simulations of $N = 1000$ particles evolving according to the system of SDEs (1). We use the Euler-Maruyama numerical scheme, with time step $dt = 0.01$, and solve for long times to ensure that the solution has converged to its invariant measure.

We also solve numerically the Fokker-Planck equation (4), subject to the boundary conditions of zero particle flux through the boundaries of our numerical interval. We approximate the derivative with a pseudo-spectral Chebyshev collocation method, and the integral term with a Clenshaw-Curtis quadrature [47]. For marching in time, we adopt the ode15s function of MATLAB, which is based on an implicit scheme combining backward differentiation and adaptive time stepping.

3 Results of numerical simulations

We now present numerical results for bifurcation diagrams and certain time-dependent simulations using the methodologies described above. The results are obtained for the three types of polynomials listed in Section 2.1.

3.1 Polynomial potentials

Here we consider confining potentials of the form

$$V(x) = \sum_{\ell=1}^M a_{\ell} x^{2\ell}, \quad (19)$$

where $M = 2, 3, \dots$. This introduces additional wells in the confining potential, corresponding to different local minima-maxima in the potential, which in turn translates into various pitchfork and/or saddle-node bifurcations from the mean-zero solution, with the corresponding changes in stability, as will be seen below.

As mentioned earlier, if $V(x)$ is a polynomial, we can obtain a system of ODEs verified by the moments $f(x) = x^k$, in a similar manner to what was presented in [13] for the bistable potential

$V(x) = \frac{x^4}{4} - \frac{x^2}{2}$ and which easily extends to arbitrary polynomial potentials. To this end, we consider the system of SDEs (1) with $W(x) = \frac{x^2}{2}$, and by defining $m_k(t) = \frac{1}{N} \sum_{\ell=1}^N (X_t^\ell)^k$, we rewrite it as

$$dX_t^i = -V'(X_t^i) dt + \theta(m_1(t) - X_t^i) dt + \sqrt{2\beta^{-1}} dB_t^i, \quad (20)$$

$i = 1, \dots, N$. Using Itô's Lemma, we can obtain a system of SDEs for the moments $f(x) = x^k$:

$$dx^k(t) = k \left[-\theta x^k(t) + (\theta m_1(t) - V'(x(t))) x^{k-1}(t) + \beta^{-1}(k-1)x^{k-2}(t) \right] dt + \sqrt{2\beta^{-1}} k x^{k-1} dw(t), \quad (21)$$

where $w(t)$ is white noise. Replacing V by its expression, noticing that $m_0(t) = 1$, and taking expectations, we obtain a system of ODEs for $m_k(t)$, $k = 1, 2, \dots, \infty$. Unfortunately, due to the structure of the potentials and the nonlinearity involved, this cannot be expanded for other types of potentials.

In the so-called ferromagnetic case, $V(x) = V_4(x) = \frac{x^4}{4} - \frac{x^2}{2}$, we obtain the following system of ODEs:

$$\dot{m}_k(t) = k \left((1 - \theta)m_k(t) + \theta m_1(t)m_{k-1}(t) + \beta^{-1}(k-1)m_{k-2}(t) - m_{k+2}(t) \right) \quad (22)$$

Other examples include higher degree polynomials:

$$V_6(x) = h(x^6 - 5x^4 + 4x^2) = hx^2(x^2 - 1)(x^2 - 4), \quad (23)$$

$$V_8(x) = h(x^8 - 14x^6 + 49x^4 - 36x^2) = hx^2(x^2 - 1)(x^2 - 4)(x^2 - 9), \quad (24)$$

where we have added a pre-factor h in the higher degree polynomials. This is to make the barrier at $x = 0$ (and/or others) more relevant. For the 6th degree case, we obtain the following system of ODEs for the moments m_k :

$$\dot{m}_k = k \left(-(8h + \theta)m_k + \theta m_1 m_{k-1} + \beta^{-1}(k-1)m_{k-2} + 20hm_{k+2} - 6hm_{k+4} \right), \quad (25)$$

and in the 8th degree case

$$\dot{m}_k = k \left((72h - \theta)m_k + \theta m_1 m_{k-1} + \beta^{-1}(k-1)m_{k-2} - 196hm_{k+2} + 84hm_{k+4} - 8hm_{k+6} \right). \quad (26)$$

We truncate the system at $k = 21$ and solve for the first moment, performing arclength continuation.

As an illustration of our methods, we plot in Fig. 4 a bistable potential $V(x) = \frac{x^4}{4} - \frac{x^2}{2}$ and the corresponding bifurcation diagram of m as a function of β . We used both arclength continuation for the self-consistency equation and the method of moments, as well as the free-energy method, obtaining similar results in all cases.

In Fig. 4, we illustrate our free-energy method to obtain the bifurcation diagram. We fix $\theta = 0.5$ and compute the free-energy surface for functions $p(x; m, \theta, \beta)$ given by (10) (without assuming that m verifies (11)) and proceed to compute its extrema, which are contoured below.

We present one more example of a polynomial confining potential, where $V(x) = V_8(x)$ from Eq. (24). We fix $h = 0.001$ and compute the bifurcation diagram of m as a function of β for $\theta = 1.5$ (5(a)) and $\theta = 2.5$ (5(b)). We observe that the topology of the bifurcation diagram is different for the two values of θ : for small θ the effects of the interaction do not affect the convexity of the free energy and we find three pitchfork bifurcations from the mean-zero solution with the corresponding (expected) changes in (linear/local) stability of all the solutions. However, for large enough θ , the effects of the interaction change the convexity of the free-energy functional, and we find only one

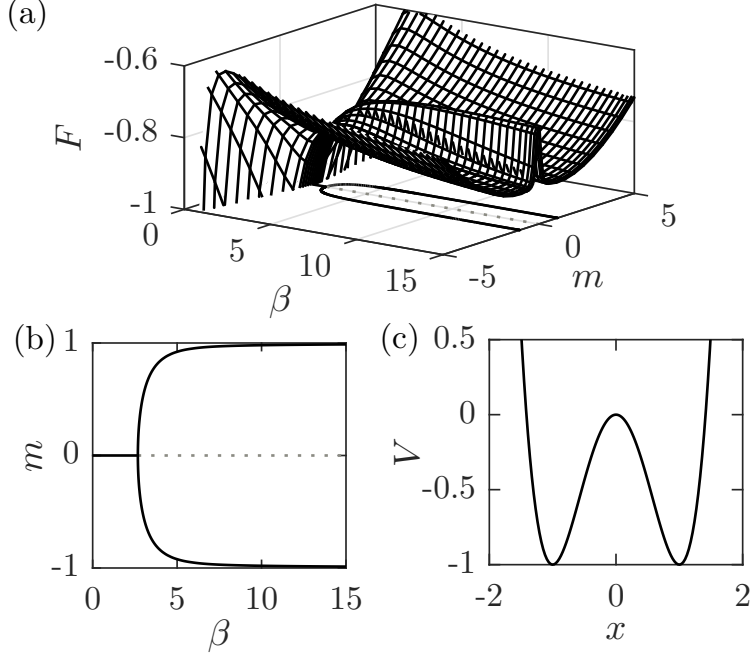


Figure 4: Free energy surface (a) and the corresponding bifurcations of the steady states of the Fokker-Planck equation (b) in a simple bi-stable potential $V(x) = \frac{x^4}{4} - \frac{x^2}{2}$ (c). The control parameter is β , and the solution norm is given by the first moment m , with $\theta = 0.5$. In (a) and (b), solid and dotted lines correspond to stable and unstable steady states of the Fokker-Planck equation, respectively.

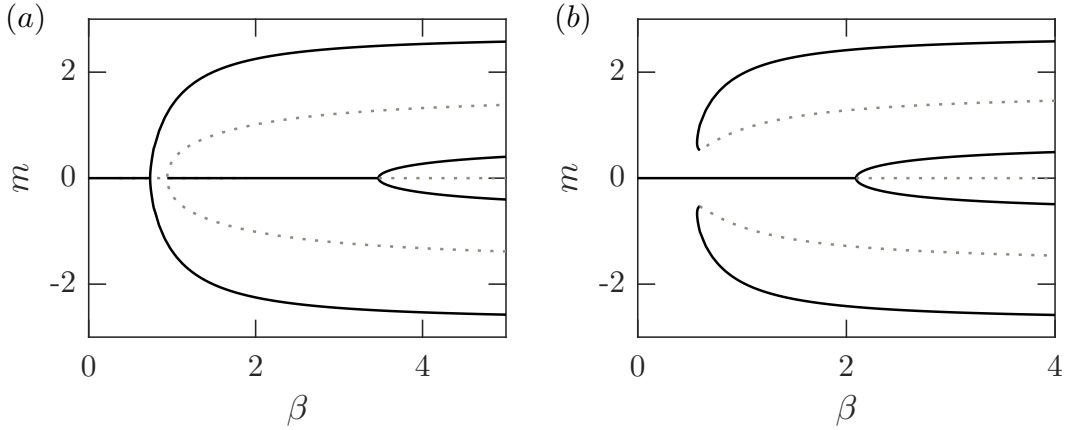


Figure 5: Phase diagram in the β - m space, for the potential $V_8(x)$, at $\theta = 1.5$ (a) and $\theta = 2.5$ (b). Solid and dotted branches are, respectively, stable and unstable steady states of the Fokker-Planck equation.

pitchfork bifurcation, accompanied by two saddle-node bifurcations. We observe, however, that the number of solutions for large β is still 7, which is the number of equilibrium points of the confining potential V_8 . In fact this is found for all the confining potentials studied in this work.

The effect of θ in the topology of the bifurcation diagram can be further analyzed by studying the critical temperature β_C at which a pitchfork bifurcation from the mean-zero solution occurs, as a function of θ . This is given by Eq. (12). We solve this equation for β_C as a function of θ again performing arclength continuation, and plot the results in Fig. 6.

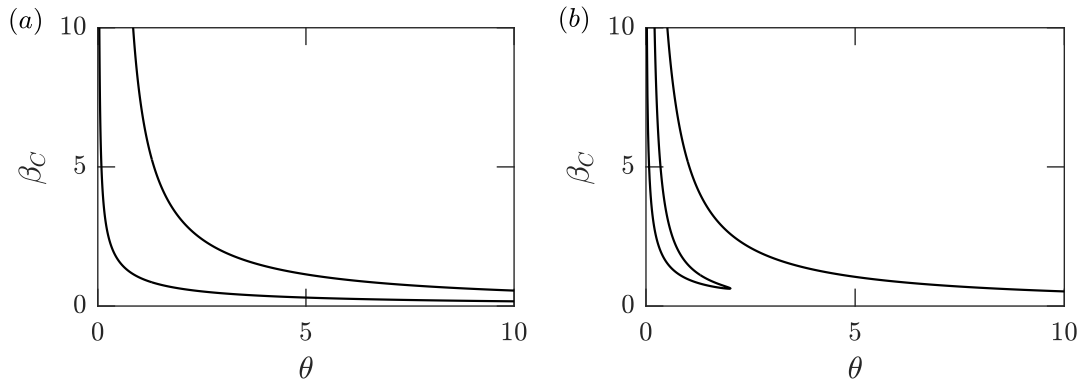


Figure 6: Critical temperature β_C as a function of θ for the potentials $V_6(x)$ with $h = 0.1$ (left panel) and $V_8(x)$ with $h = 0.001$ (right panel) given by Eqs (23) and (24) respectively.

We also see the existence of two branches for the 6th degree polynomial potential, which corresponds, as expected, to the existence of two pitchfork bifurcations in the bifurcation diagram of the first moment, m , as a function of the inverse temperature β . Interestingly, for the 8th degree polynomial, there are three branches of solutions for sufficiently small θ but these branches merge for $\theta \approx 2$. This indicates that the convexity of the free-energy functional changes as a function of θ , which also means that for polynomial potentials it is important to keep track of the bifurcation structure as a function of both β and θ . This change of convexity leads to the behavior observed in Fig. 5: for small enough θ (Fig. 5(a)) there exist three pitchfork bifurcations, with the corresponding change of stability in the mean-zero solution, while for large values of θ (Fig. 5(b)) there is only one pitchfork bifurcation, with the $m = 0$ solution remaining the global minimum of the free-energy for larger values of β . The other stationary solutions still exist, but they appear as discontinuous bifurcations (corresponding to first-order phase transitions).

Finally, we study the effect of breaking the symmetry of polynomial potentials by adding a tilt to a bistable potential. Specifically, we consider potentials of the form

$$V(x) = \frac{1}{a_0} \left(\frac{x^4}{4} - \frac{x^2}{2} \right) + \kappa x. \quad (27)$$

Fig. 7 depicts the bifurcation diagram of m as a function of β for this potential, with $\theta = 2.5$, $a_0 = 0.249998581434761$, and $\kappa = 0, 0.01, 0.1, 1$. Evidently a break in the symmetry of the bifurcation diagram appears, which becomes increasingly clear as κ increases.

The existence of stationary solutions raises the question of relevance of these solutions which is related to the way they attract initial conditions. An answer to this question can be given by means of time-dependent computations. Figs. 8 and 9 depict the time evolution of the first moment as a function of time (top panel) and the histogram and corresponding distribution (solution of the time dependent Fokker–Planck equation) in the bottom panel, at two selected times marked in dashed lines in the top panel. Both figures correspond to the tilted bistable potential given by

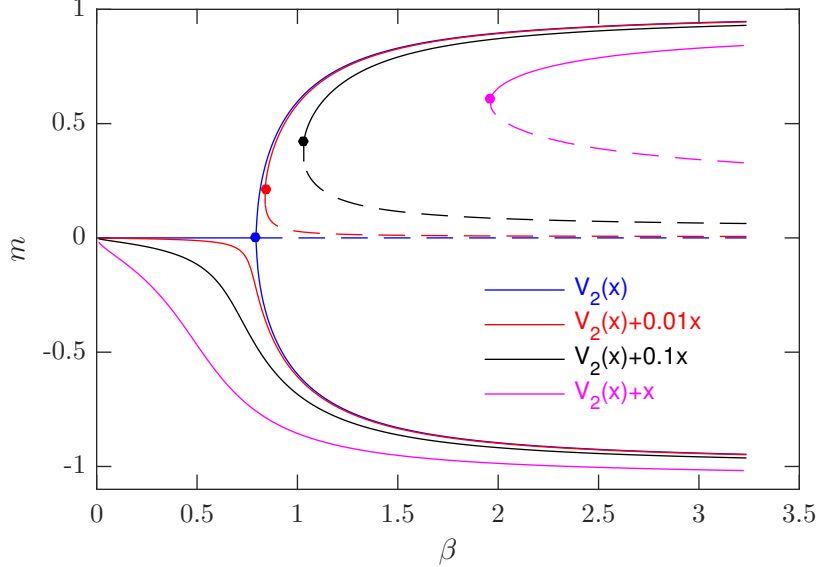


Figure 7: Bifurcation diagrams of m as a function of β for tilted bistable potentials given by Eq. (27) with $a_0 = 0.249998581434761$, and $\kappa = 0, 0.01, 0.1, 1$ (see legend). Here, we used $\theta = 2.5$. The symmetric pitchfork bifurcation is broken at any $\kappa > 0$. We note that the locus of the critical points forms a distinct critical line.

Eq. (27) with $\kappa = 0.1$, $\theta = 2.5$ and $\beta = 1.5$. Fig. 8 shows the evolution starting from a $N(0.1, \beta^{-1})$, while in Fig. 9 the time evolution is started from a $N(-0.1, \beta^{-1})$ distribution.

An overall good agreement is observed between the solution of the time dependent Fokker–Planck equation and the corresponding MC simulations. It is worth noting that, without the tilt, the dynamics reproduced in Fig. 8 would have evolved to the upper branch of the bifurcation diagram represented in Fig. 7, but instead we observe the breaking of symmetry caused by the tilt: the particles would have to pass through an unstable equilibrium point (represented by a black dashed line in Fig. 7) in order to reach the upper branch.

3.2 Rational potentials

Here, we consider potentials of the form

$$V(q) = \frac{1}{\sum_{\ell=-N}^N \delta_{\ell}|q - c_{\ell}q_{\ell}|^{-2}}. \quad (28)$$

with both deterministic and random distributions of $\{\delta_{\ell}, c_{\ell}\}$. We show two examples in particular. The first one is a potential with 6 minima, which are symmetrically located and have the same depths (as well as heights of the corresponding local maxima),

$$V(x) = h \left((x-1)^{-2} + (x+1)^{-2} + (x-2)^{-2} + (x+2)^{-2} + (x-3)^{-2} + (x+3)^{-2} \right)^{-1}. \quad (29)$$

The free energy surface and bifurcation diagram for this case are presented in Fig. 10.

We now consider the potential from Eq. (28) with $N = 20$ minima positioned at $x = -10, -9, \dots, 10$, and $c_{\ell} = 1$, $\ell = 1, \dots, 20$. Fig. 11 depicts the realization of a random potential, where the energy

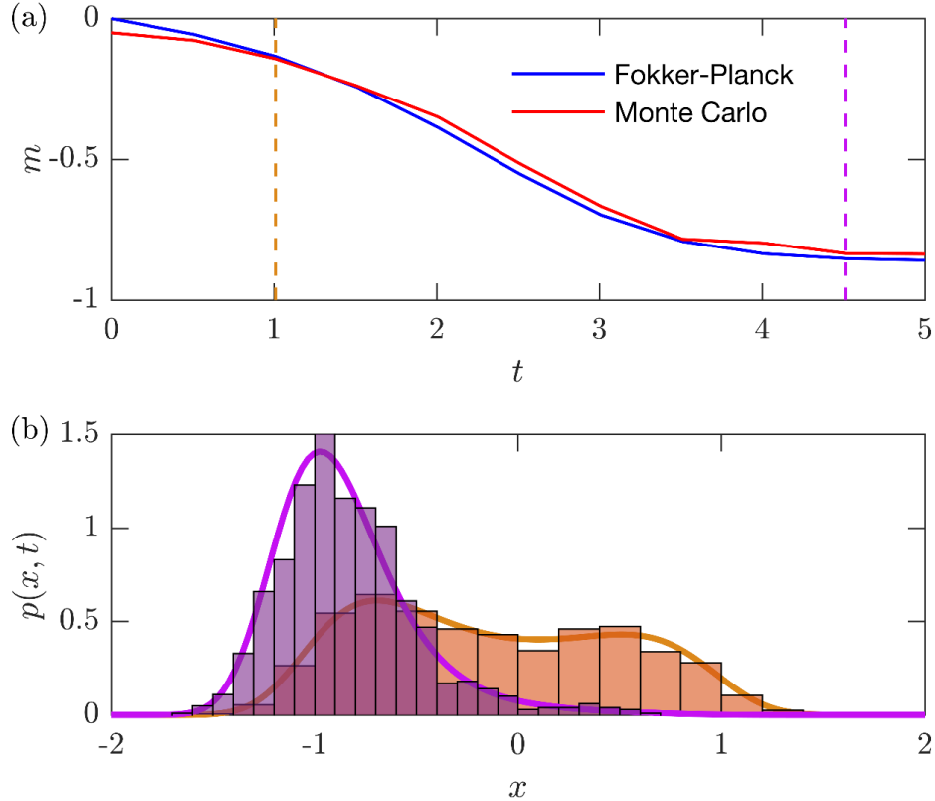


Figure 8: Evolution of the density and first moment in a tilted bistable potential given in Eq. (27), with $\kappa = 0.1$ and an initial condition distributed according to a $N(0, \beta^{-1})$ distribution. (a) Mean position against time for the evolution of the Fokker–Planck equation (blue line) and for the interacting particles system (red line). (b) Fokker–Planck distributions and corresponding MC histograms for selected times, designated in (a) by vertical dashed lines of respective colors (see also the Supplemental Material movies `MovM1.avi`, showing simultaneously the first moment on the bifurcation diagram and the distribution, and `MovFig8.avi`, showing the good agreement between Fokker–Planck and MC simulations).

barriers separating the local minima of the potential are uniformly distributed random variables, i.e. $\delta_\ell \sim U([0, 1])$.

Interestingly, the random depths of each local minima – these correspond to higher or lower energy barriers – affect the stability of each well with respect to each other. Further insight into the effect of the random depths on the dynamics of the system can be obtained via the time-dependent evolution of both the particle system and the mean-field Fokker–Planck equation. The corresponding results are plotted in Figs. 12 and 13.

Fig. 12 shows the solution of the Fokker–Planck equation as a function of time for four different times (top panel), and the corresponding location of the mean of the solution at each of these times on the bifurcation diagram (lower panel). We have introduced an empirical “convergence” time t_∞ , defined as the time at which the relative norm between the time-dependent solution and the steady state is less than 5%:

$$\|p_\infty(x) - p(x, t_\infty)\| \leq 0.05 \|p_\infty(x)\|, \quad (30)$$

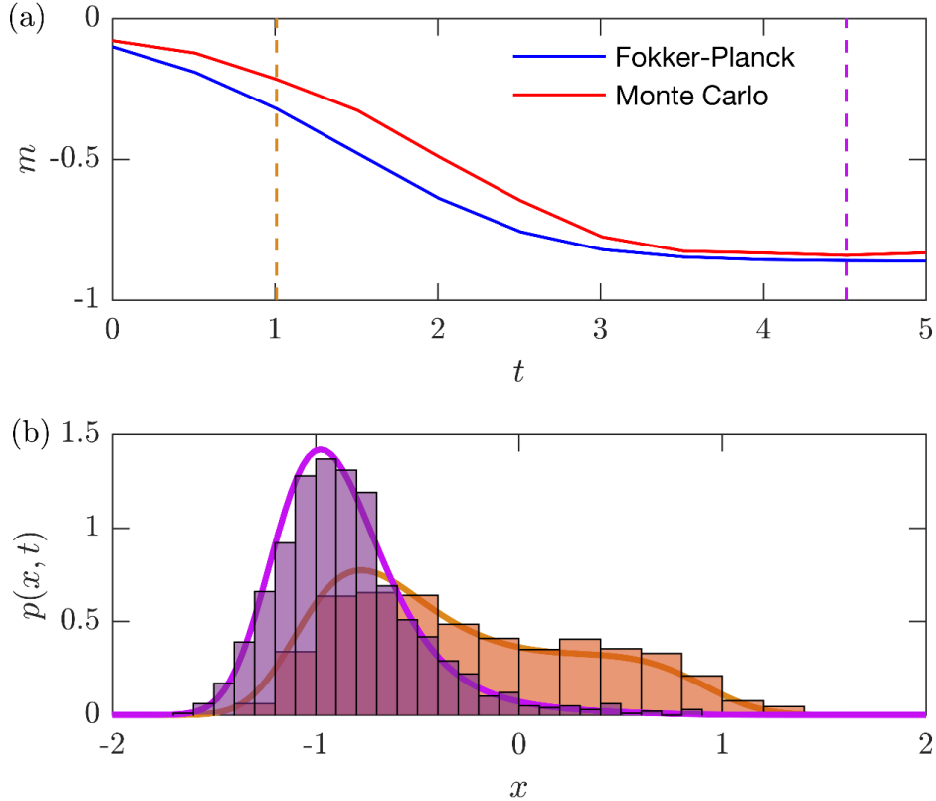


Figure 9: Evolution of the density and first moment in a tilted bistable potential given in Eq. (27), with $\kappa = 0.1$ and an initial condition distributed according to a $N(-0.1, \beta^{-1})$ distribution. (a) Mean position against time for the evolution of the Fokker–Planck equation (blue line) and for the interacting particles system (red line). (b) Fokker–Planck distributions and corresponding Monte–Carlo histograms for selected times, designated in (a) by vertical dashed lines of respective colors (see also movie `MovFig9.avi` in Supplemental Material showing good agreement between Fokker–Planck and MC simulations).

where $\|\cdot\|$ stands for the Euclidean norm over \mathbb{R} . It should be noted that as we approach the turning points of the bifurcation diagram in Fig. 12(b), by e.g. fixing β and increasing m , the system slows down and eventually “freezes” and gets pinned to the branch of metastable solutions, which terminates at the turning point. Hence, in the neighborhood of turning points, we have a “glass”-like behavior (e.g. [5]), and the potential in Fig. 11 can be viewed as a “glassy potential”. Movie `MovM1.avi` in the Supplemental Material shows such a pinning transition for a tilted bistable potential, which clearly occurs at the boundary of the basin of attraction of the upper U-branch. For model prototype systems, such as the Swift–Hohenberg equation, the time between two consecutive transitions can be estimated via weakly-nonlinear analysis in the vicinity of the turning points [9]. But our equations are too involved to be amenable to analytical treatment of this type.

We can explore the behavior in Fig. 12 further by plotting the first moment of the solution as a function of time – we do so in Fig. 13. The top panel displays the first moment as a function of time for the solution of the Fokker–Planck equation (full blue line) compared with two independent runs of the particle system. while the bottom panel compares the Fokker–Planck solution with

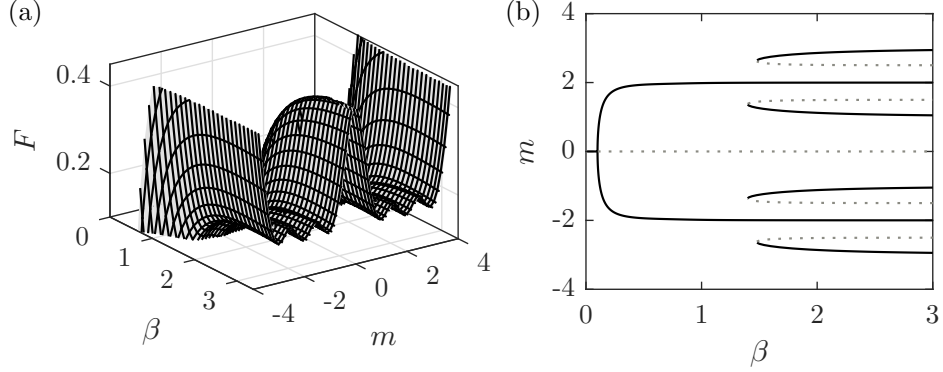


Figure 10: Free energy surface (a) and the corresponding bifurcation diagram in the β - m parameter space (b) for the potential in Equation (29) with $\theta = 5$ and $h = 1$. Stable and unstable branches are plotted with solid and dotted lines respectively.

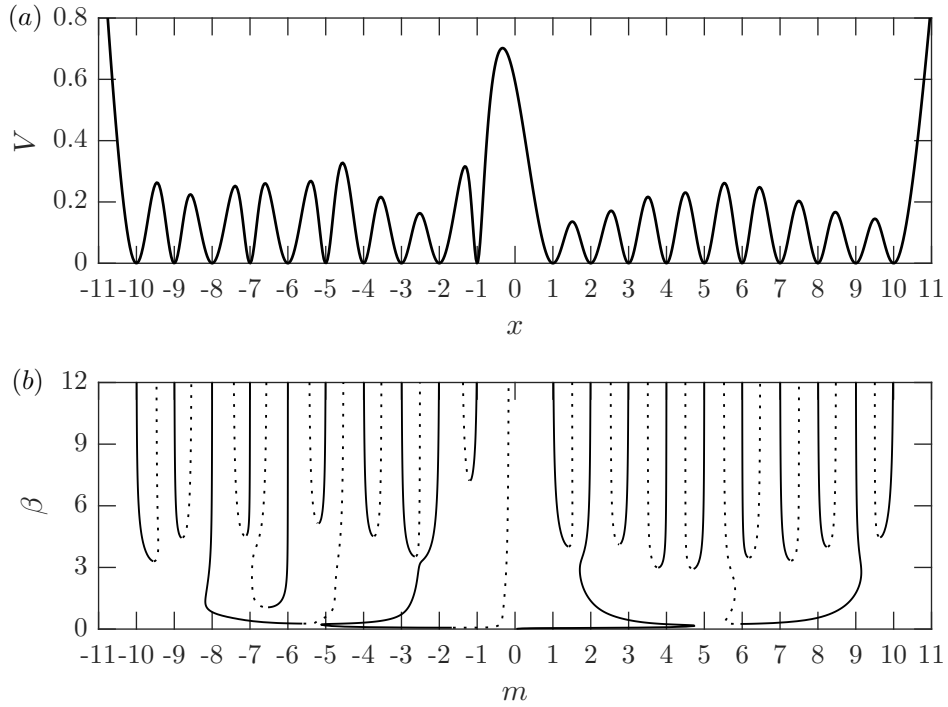


Figure 11: (a) A potential from Equation (28), with the minima positioned at integers between -10 and 10, separated by local maxima of arbitrary heights. (b) Corresponding bifurcation diagram of the steady states of the Fokker-Planck Equation (4), obtained from the computed free-energy surface. Stable and unstable states are designated by solid and dashed curves, respectively.

the histograms from the particle simulations. Each particle run had $N = 1000$ particles and the simulations shown use $\theta = 1.5$ and $\beta \approx 2.66$.

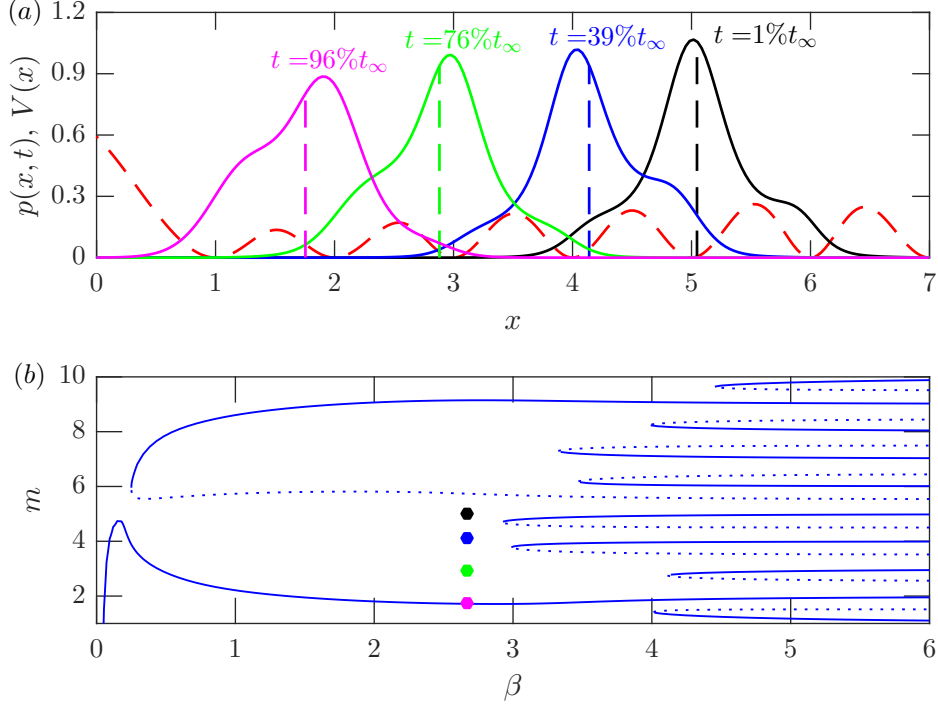


Figure 12: Numerical solution of the Fokker-Planck equation (4), for the potential given in Fig. 11 (see also MovFig12.avi in the supplemental material). (a) $p(x,t)$ (solid curves) and $V(x)$ (dashed curve). The first moments for each $p(x,t)$ are designated by dashed verticals, and the respective values of t are provided. (b) States from (a) on the bifurcation diagram. We note that the basins of attraction of the stable states are effectively demarcated by the metastable branches of the bifurcation diagram. Here t_∞ is the time upon which the relative norm of the difference between the steady state and the time-dependent solution is less than 5%.

3.3 Piecewise linear potentials with quadratic growth at infinity

Here we will replace the confining potential with a piecewise linear approximation with quadratic growth at infinity. Our motivation for this is that we can now compute the partition function $Z(m, \theta, \beta)$, the mean $R(m)$ and the variance analytically (in terms of the error function $\text{erf}(x) = \frac{2}{\sqrt{\pi}} \int_0^x e^{-x^2} dx$). We consider a potential V with $2M$ local minima, $X = (x_1, \dots, x_{2M})$, with depth h_i , and the local maxima, located at $x_{i+\frac{1}{2}} = \frac{x_i + x_{i+1}}{2}$ (note that $x_{-1/2} = 0$), have height H_i . In this case, V is given by

$$V(x) = \begin{cases} \frac{x^2 - x_1^2}{2} + h_1, & x \leq x_1, \\ \frac{(H_i - h_i)x}{x_{i+\frac{1}{2}} - x_i} + \frac{h_i x_{i+\frac{1}{2}} - H_i x_i}{x_{i+\frac{1}{2}} - x_i}, & x_i < x < x_{i+\frac{1}{2}}, \\ \frac{(h_i - H_i)x}{x_{i+1} - x_{i+\frac{1}{2}}} + \frac{H_i x_{i+1} - h_i x_{i+\frac{1}{2}}}{x_{i+1} - x_{i+\frac{1}{2}}}, & x_{i+\frac{1}{2}} < x < x_{i+1}, \\ \frac{x^2 - x_{2M}^2}{2} + h_{2M} & x \geq x_{2M}. \end{cases} \quad (31)$$

$i = 1, \dots, 2M$.

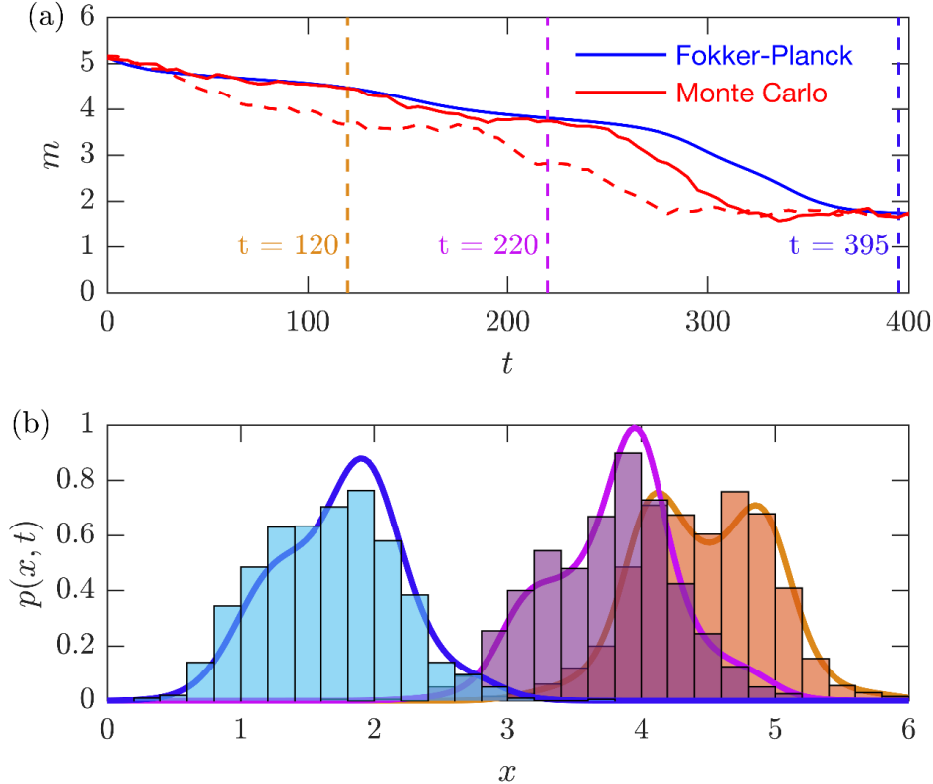


Figure 13: Same as in Fig. 12, against the corresponding Monte–Carlo simulation data. (a) Mean position against time for the evolution of the Fokker–Planck equation (full blue line) and the interacting particles system for two realisations of the noise (full and dashed red lines). (b) Fokker–Planck distributions and corresponding Monte Carlo histograms for selected times, designated in (a) by vertical dashed lines of respective colors. We can see an overall good agreement between the simulations and computations.

As mentioned before, we can compute the quantities $Z(m, \theta, \beta)$, $R(m)$ and the second moment analytically, and will present two illustrative cases: a symmetric potential with $2M = 6$ wells and a non-symmetric potential with random heights and depths. Details of the analytical calculations are given in Appendix A.

3.3.1 Symmetric potentials with six wells at same heights

Below we present the results for $V(x)$ given by Eq. (31) with $M = 3$. We use $X = (-3, -2, -1, 1, 2, 3)$, $x_{i+\frac{1}{2}} = \frac{x_i + x_{i+1}}{2}$, $h_i = 0$, and $H_i = 1$. We compute $Z(m, \theta, \beta)$ and $R(m)$ using Eqs (33) and (34) respectively, and solve for $R(m) = m$ using arclength continuation. We plot our results in Fig. 14. Here, we choose $\theta = 5$. Panel (a) shows the solution of the self-consistency equation $R(m) = m$ (or, rather $R(m) - m = 0$) for $\beta = 1$ and 10. Panel (b) shows the bifurcation diagram of m as a function of β and (c) shows the critical temperature β_C as a function of θ , which was obtained using Eq. (35) for $m = 0$.

The results are what we would expect: there are eleven equilibrium points which correspond to

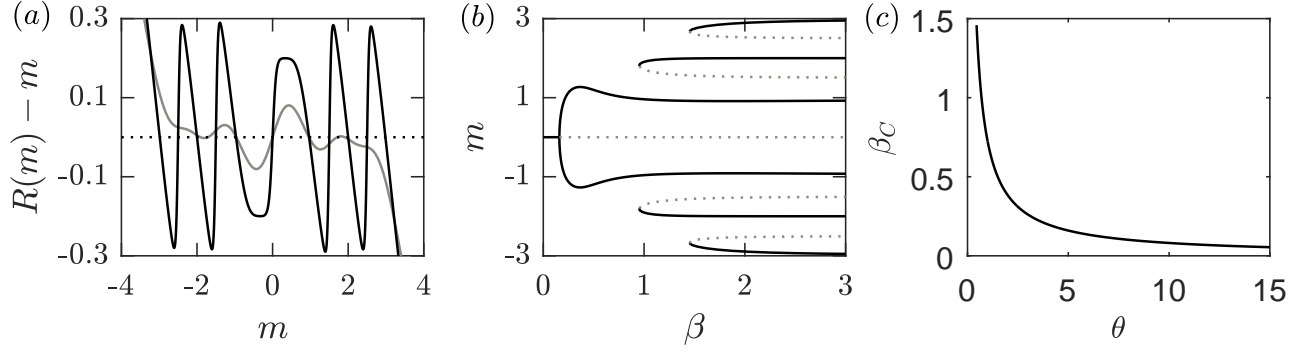


Figure 14: Phase diagram for the case of the piecewise linear potential (31) with 6 wells for $\theta = 5$. Panel (a) shows the solution of $R(m) - m = 0$ for $\beta = 1$ (black) and $\beta = 10$ (grey). Horizontal dotted line is drawn at $R(m) - m = 0$. Panel (b) shows the bifurcation diagram in the β - m space. Panel (c) shows the critical temperature β_C at which a pitchfork bifurcation occurs from the mean-zero solution as a function of θ .

each local minimum and maximum. We point out the similarity between the bifurcation diagram in panel (b) to the one presented in Fig. 10, which shows that a piecewise linear potential is a good first approximation.

3.3.2 Potentials with four wells at different (randomly distributed) heights

Our final test is the case where $V(x)$ is given by Eq. (31) with $M = 2$, but with the minima and maxima heights and depths randomly distributed. We use, $X = (-2, -1, 1, 2)$, $x_{i+\frac{1}{2}} = \frac{x_i + x_{i+1}}{2}$, and generated h_i and H_j , $i = 1, \dots, 4$, $j = 1, \dots, 3$ randomly, following a uniform distribution.

As before, we compute the relevant functions of m , θ and β using Eqs (33)-(35) and depict in Fig. 15 the solution of $R(m) - m = 0$ for $\beta = 1, 10$ and $\theta = 5$ (panel (a)), the bifurcation diagram of m as a function of β for $\theta = 5$ and the critical temperature β_C as a function of θ .

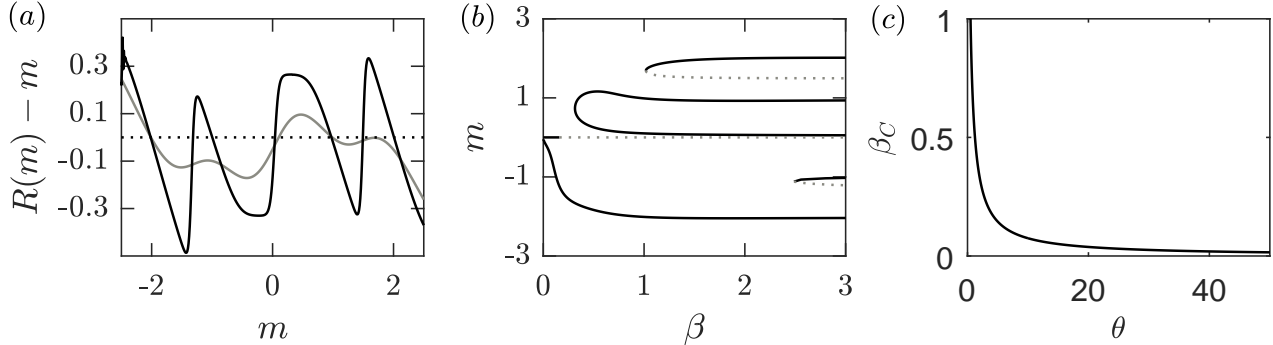


Figure 15: Phase diagram for the case of the piecewise linear potential (31) with 4 wells at random heights and depths for $\theta = 5$. Panel (a) shows the solution of $R(m) - m = 0$ for $\beta = 1$ (black) and $\beta = 10$ (grey). Horizontal dotted line is drawn at $R(m) - m = 0$. Panel (b) shows the bifurcation diagram in the β - m space. Panel (c) shows the critical temperature β_C at which a pitchfork bifurcation occurs from the mean-zero solution as a function of θ .

A behavior similar to that of the random potential in the previous section is observed but with a smaller number of equilibrium points.

4 Conclusions

We presented a detailed and systematic investigation of the dynamics of a system of interacting particles in one dimension, moving in a confining multi-well potential and interacting through a Curie-Weiss/quadratic potential. Passing formally to the mean-field limit yields the McKean SDE. The Fokker-Planck equation corresponding to this SDE is the McKean-Vlasov equation, which is nonlocal and nonlinear, and is the basic equation for our study. It is a gradient-flow for a certain free-energy functional, establishing also a connection with thermodynamics.

A wide spectrum of prototypical model potentials was considered: polynomial (including tilted bistable ones), rational (both deterministic and random) and piecewise linear potentials with quadratic growth at infinity that allow for analytical estimates of the partition function, mean and variance. For all these model potentials, we scrutinized steady states of the McKean-Vlasov equation, constructed bifurcation diagrams and studied their behavior in the parameter space, and determined the stability of the solution branches. We also determined the critical points and characterized the structure and nature of phase transitions. We showed, by means of extensive computations – including free-energy minimization, arclength continuation, simulations of the full McKean-Vlasov equation, and MC simulations of the corresponding particle system – and of analytical calculations for explicitly solvable models, that the number of steady states, their stability and structure of bifurcation diagrams depends crucially on the form of the multi-well potential and its characteristics, mainly the number and depth of the local minima of the confining potential. Increasing the complexity of the potential increases also the complexity of the steady-state bifurcation structure and dynamics. Even the local minima of the potential may significantly affect the relaxation dynamics of the system, via the basin of attraction of the metastable states. Thus, each local minima of the potential gives rise to a pair of branches (stable and unstable) of the steady state bifurcation diagram. These branches merge at the critical point, associated with the respective potential minimum. It is also encouraging that the mean-field Fokker-Planck equation is in remarkable agreement with the MC simulations of the system dynamics.

There are also several new avenues of research. Indeed, we believe that the theoretical-computational framework and associated methodologies presented here can be useful for the study of bifurcations and phase transitions for more complicated physical systems. Or indeed for systems where the potential is known from experiments only, either physical or in-silico ones, and then our framework can be adopted in a “data-driven” approach. Of particular interest would also be extension to multi-dimensional problems. Two-dimensional problems in particular would be of direct relevance to surface diffusion and therefore to technological processes in materials science and catalysis. Other interesting extensions include additional effects and complexities such as non-Markovian interaction particles, colored and multiplicative noise and nonreversible perturbations [30, 16]. Recall also from the Introduction, that our starting point, a system of interacting particles in a confining potential, retains the main features of DDFT models. Another interesting study would then be applications of our framework to such models. Finally, the study of phase transitions for the stochastic gradient descent dynamics algorithms and of their mean field limit that are used in the training of neural networks is an intriguing problem, with important potential applications. We shall examine these and related questions in future studies.

Acknowledgements

We are grateful to Ch. Kuehn for useful discussions, particularly about the method of moments. We acknowledge financial support from the Engineering and Physical Sciences Research Council (EPSRC) of the UK through Grants No. EP/L027186, EP/L020564/1, EP/K034154/1, EP/P031587/1, EP/L024926/1 and EP/L025159/1.

A Formulas for $Z(m)$, $R(m)$ and $V(m)$, for piecewise linear potentials with quadratic growth

Here we list the values of $Z(m)$, $R(m)$ and $V(m)$ for a potential of the form in Section 3.3. We consider a general potential with $2M$ minima which have heights h_1, \dots, h_{2M} and are located at x_1, \dots, x_{2M} . There are, therefore, $2M - 1$ maxima/barriers H_i , $i = 1, \dots, 2M - 1$, located at y_i . Throughout our study we take $y_i = \frac{x_i + x_{i+1}}{2}$, but the formulas are valid in the general case. We define

$$\alpha = \sqrt{\frac{\beta}{2\theta}}, \quad \gamma = \sqrt{\frac{\beta}{2(\theta + 1)}},$$

$$s_i = \frac{H_i - h_i}{x_i - x_{i+1}}, \quad S_i = \frac{H_i - h_{i+1}}{x_i - x_{i+1}},$$

and $f(\zeta, x, s) = \text{erf}(\zeta(\theta(m - x) + s))$ (32)

Using these, we obtain

$$\begin{aligned} Z(m) = & -\frac{\sqrt{\pi}}{\beta} \left\{ \alpha e^{(\alpha m \theta)^2} \left[\sum_{i=1}^{2M-1} (f(\alpha, y_i, 2s_i) - f(\alpha, x_i, 2s_i)) e^{4\alpha^2 \left(\frac{(h_i(y_i - m) + H_i(m - x_i))\theta}{x_i - x_{i+1}} + s_i^2 \right)} \right. \right. \\ & \left. \left. - \sum_{i=1}^{2M-1} (f(\alpha, y_i, -2S_i) - f(\alpha, x_{i+1}, -2S_i)) e^{4\alpha^2 \left(\frac{(h_{i+1}(m - y_i) + H_i(x_{i+1} - m))\theta}{x_i - x_{i+1}} + S_i^2 \right)} \right] \right. \\ & \left. + \gamma e^{(\gamma m \theta)^2} \left((f(\gamma, x_1, -x_1) - 1) e^{\gamma^2(x_1^2 - 2h_1)(\theta + 1)} - e^{\gamma^2(x_{2M}^2 - 2h_{2M})(\theta + 1)} (f(\gamma, x_{2M}, -x_{2M}) + 1) \right) \right\} \end{aligned} \quad (33)$$

$$\begin{aligned} R(m) = & \frac{\left(e^{\beta(x_1(m - \frac{x_1}{2})\theta - h_1)} - e^{\beta(x_{2M}(m - \frac{x_{2M}}{2})\theta - h_{2M})} \right)}{\theta(\theta + 1)\beta Z(m)} + \frac{\sqrt{\pi}}{\beta Z(m)} \times \\ & \times \left[\frac{\alpha}{\theta} \left\{ \sum_{i=1}^{2M-1} (\theta m - 2S_i) (f(\alpha, y_i, -2S_i) - f(\alpha, x_{i+1}, -2S_i)) e^{-4\alpha^2 \left(\frac{(h_{i+1}(y_i - m) + H_i(m - x_{i+1}))\theta}{x_i - x_{i+1}} - S_i^2 \right)} \right. \right. \\ & \left. \left. - \sum_{i=1}^{2M-1} (\theta m + 2s_i) (f(\alpha, y_i, 2s_i) - f(\alpha, x_i, 2s_i)) e^{4\alpha^2 \left(\frac{(h_i(y_i - m) + H_i(m - x_i))\theta}{x_i - x_{i+1}} + s_i^2 \right)} \right\} e^{(\alpha m \theta)^2} \right. \\ & \left. + \frac{\gamma m \theta e^{(\gamma m \theta)^2}}{(\theta + 1)} \left\{ (f(\gamma, x_1, -x_1) - 1) e^{\gamma^2(x_1^2 - 2h_1)(\theta + 1)} - (f(\gamma, x_{2M}, -x_{2M}) + 1) e^{\gamma^2(x_{2M}^2 - 2h_{2M})(\theta + 1)} \right\} \right] \end{aligned} \quad (34)$$

$$\begin{aligned}
V(m) &= -e^{\beta(x_1(m-\frac{x_1}{2})\theta-h_1)} \frac{(m+x_1)\theta+x_1}{(\theta+1)^2\beta Z(m)} + e^{\beta(x_{2M}(m-\frac{x_{2M}}{2})\theta-h_{2M})} \frac{(m+x_{2M})\theta+x_{2M}}{\beta(\theta+1)^2 Z(m)} \\
&- \frac{\sqrt{\pi}\gamma(\beta\theta^2 m^2 + \theta + 1)e^{(\gamma m\theta)^2}}{(\theta+1)^2\beta^2 Z(m)} \left[(f(\gamma, x_1, -x_1) - 1)e^{\gamma^2((x_1^2-2h_1)(\theta+1))} - (f(\gamma, x_{2M}, -x_{2M}) + 1)e^{\gamma^2((x_{2M}^2-2h_{2M})(\theta+1))} \right] \\
&+ \frac{\sum_{i=1}^{2M-1} ((m+x_i)\theta + 2s_i)e^{\beta(x_i(m-\frac{x_i}{2})\theta-h_i)} - ((m+x_{i+1})\theta - 2S_i)e^{\beta(x_{i+1}(m-\frac{x_{i+1}}{2})\theta-h_{i+1})} - 2(s_i + S_i)e^{\beta(y_i(m-\frac{y_i}{2})\theta-H_i)}}{\theta^2\beta Z(m)} \\
&- \frac{\sqrt{\pi}\alpha e^{(\alpha m\theta)^2}}{\theta^2\beta^2 Z(m)} \left(\sum_{i=1}^{2M-1} (f(\alpha, y_i, 2s_i) - f(\alpha, x_i, 2s_i)) (\beta\theta^2 m^2 + \theta + 4\beta s_i(m\theta + s_i)) e^{4\alpha^2 \left(\frac{(h_i(y_i-m)+H_i(m-x_i))\theta}{x_i-x_{i+1}} + s_i^2 \right)} \right. \\
&\left. - \sum_{i=1}^{2M-1} (f(\alpha, y_i, -2S_i) - f(\alpha, x_{i+1}, -2S_i)) (\beta\theta^2 m^2 + \theta - 4\beta S_i(m\theta - S_i)) e^{-4\alpha^2 \left(\frac{(H_i(m-x_{i+1})+h_{i+1}(y_i-m))\theta}{x_i-x_{i+1}} - S_i^2 \right)} \right)
\end{aligned} \tag{35}$$

References

- [1] S. Adams, N. Dirr, M. Peletier and J. Zimmer. Large deviations and gradient flows. *P. Roy. Soc. A-Math. Phys.*, 371(2005):20120341, 2013.
- [2] E. L. Allgower and K. Georg. *Introduction to Numerical Continuation Methods*. Colorado State University, 1990.
- [3] N. Bain and D. Bartollo. Critical mingling and universal correlations in model binary active liquids. *Nat. Commun.*, 8:15969, 2017.
- [4] R. Balescu. *Statistical dynamics. Matter out of equilibrium*. Imperial College Press, London, 1997.
- [5] L. Berthier and G. Biroli. Theoretical perspective on the glass transition and amorphous materials. *Rev. Mod. Phys.*, 83:587–645, 2011.
- [6] J. Binney and S. Tremaine. *Galactic Dynamics*. Princeton University Press, Princeton, second edition, 2008.
- [7] V.I. Bogachev, N.V. Krylov, M. Röckner, and S. V. Shaposhnikov. *Fokker-Planck-Kolmogorov equations*, volume 207 of *Mathematical Surveys and Monographs*. American Mathematical Society, Providence, RI, 2015.
- [8] S. Bonfanti and W. Kob. Methods to locate saddle points in complex landscapes. *J. Chem. Phys.*, 2017
- [9] J. Burk and E. Knobloch. Localized states in the generalized swift-hohenberg equation. *Phys. Rev. E*, 73:056211, 2006.
- [10] J.A. Carrillo, R.S. Gvalani, G.A. Pavliotis and A. Schlichting. Long-time behaviour and phase transitions for the McKean–Vlasov equation on the torus. *arXiv:1806.01719*, 2018.

- [11] J.A. Carrillo, R.J. McCann, and C. Villani. Contractions in the 2-Wasserstein length space and thermalization of granular media. *Arch. Ration. Mech. Anal.*, 179(2):217–263, 2006.
- [12] S.F. Chekmarev. Protein folding as a complex reaction: a two-component potential for the driving force of folding and its variation with folding scenario. *Plos One*, 10:0121640, 2015.
- [13] D.A. Dawson. Critical dynamics and fluctuations for a mean-field model of cooperative behavior. *J. Statist. Phys.*, 31(1):29–85, 1983.
- [14] A. Dhooge, W. Govaerts, Yu.A. Kuznetsov, W. Mestrom, A.M. Riet, and B. Sautois. *MATCONT and CL MATCONT: Continuation toolboxes in matlab*. Utrecht University, Netherlands and Universiteit Gent, Belgium, 2006.
- [15] N. Dirr, M. Stamatakis and J. Zimmer. Entropic and gradient flow formulations for nonlinear diffusion. *J. Math. Phys.*, 57(8):081505, 2016.
- [16] A.B. Duncan, T. Lelièvre and G.A. Pavliotis. Variance Reduction Using Nonreversible Langevin Samplers. *J. Stat. Phys.*, 163(3):457–491, 2016.
- [17] M.H. Duong and G.A. Pavliotis. Mean field limits for non-Markovian interacting particles: convergence to equilibrium, GENERIC formalism, asymptotic limits and phase transitions. *arXiv:1805.04959*, 2018.
- [18] F. Farkhooi and W. Stannat. A complete mean-field theory for dynamics of binary recurrent neural networks. *arXiv:1701.07128v1*, 2017.
- [19] T. D. Frank. *Nonlinear Fokker-Planck equations*. Springer Series in Synergetics. Springer-Verlag, Berlin, 2005.
- [20] J. Garnier, G. Papanicolaou, and T.-W. Yang. Large deviations for a mean field model of systemic risk. *SIAM Journal of Financial Mathematics*, 4(1):151–184, 2013.
- [21] J. Garnier, G. Papanicolaou, and T.-W. Yang. Consensus convergence with stochastic effects. *Vietnam J. Math.*, 45(1-2):51–75, 2017.
- [22] J. Gärtner. On the McKean -Vlasov limit for interacting diffusions. *Math. Nachr.*, 137:197–248, 1988.
- [23] B.D. Goddard, A. Nold, N. Savva, G.A. Pavliotis, and S. Kalliadasis. General dynamical density functional theory for classical fluids. *Phys. Rev. Lett.*, 109:120603, 2012.
- [24] B.D. Goddard, A. Nold, N. Savva, P. Yatsyshin, and S. Kalliadasis. Unification of dynamic density functional theory for colloidal fluids to include inertia and hydrodynamic interactions: derivations and numerical experiments. *J. Phys.: Condens. Matter*, 25:035101, 2013.
- [25] B.D. Goddard, G.A. Pavliotis, and S. Kalliadasis. The overdamped limit of dynamic density functional theory: rigorous results. *Multiscale Model. Simul.*, 10:633–663, 2012.
- [26] S.N. Gomes and G.A. Pavliotis. Mean field limits for interacting diffusions in a two-scale potential. *Journal of Nonlinear Science*, 28(3):905–941, 2018.

- [27] S. Kawai and T. Komatsuzaki. Hierarchy of reaction dynamics in a thermally fluctuating environment. *Phys. Chem. Chem. Phys.*, 12:7626–7635, 2010.
- [28] F.J. Keil. Multiscale modelling in computational heterogeneous catalysis. In B. Kirchner and J. Vrabec, editors, *Multiscale Molecular Methods in Applied Chemistry*, volume 307, pages 69–107. Topics in Current Chemistry, Springer, 2012.
- [29] B. Krauskopf. *Numerical Continuation Methods for Dynamical Systems*. Springer, 2007.
- [30] T. Lelièvre, F. Nier and G.A. Pavliotis. Optimal Non-reversible Linear Drift for the Convergence to Equilibrium of a Diffusion. *J. Stat. Phys.*, 152(2):237–274, 2013.
- [31] E. Luçon and W. Stannat. Transition from gaussian to non-gaussian fluctuations for mean-field diffusions in spatial interaction. *The Annals of Probability*, 26(6):3840–3909, 2016.
- [32] N. Martzel and C. Aslangul. Mean-field treatment of the many-body Fokker-Planck equation. *J. Phys. A*, 34(50):11225–11240, 2001.
- [33] H.P. McKean. Propagation of chaos for a class of non-linear parabolic equations. *Stochastic Differential Equations (Lecture Series in Differential Equations, Session 7, Catholic Univ., 1967)*, pages 41–57., 1967.
- [34] H.P. McKean, Jr. A class of Markov processes associated with nonlinear parabolic equations. *Proc. Nat. Acad. Sci. U.S.A.*, 56:1907–1911, 1966.
- [35] S. Motsch and E. Tadmor. Heterophilious dynamics enhances consensus. *SIAM Review*, 56(4):577–621, 2014.
- [36] K. Müller and L.D. Brown. Location of saddle points and minimum energy paths by a constrained simplex optimization procedure. *Theoret. Chim. Acta (Berl.)*, 53(1):75–93, 1979.
- [37] K. Oelschläger. A martingale approach to the law of large numbers for weak interacting stochastic processes. *The Annals of Probability*, 12(2):458–479, 1984.
- [38] G. A. Pavliotis. *Stochastic processes and applications*, volume 60 of *Texts in Applied Mathematics*. Springer, New York, 2014. Diffusion processes, the Fokker-Planck and Langevin equations.
- [39] G.A. Pavliotis and A.M. Stuart. *Multiscale Methods*, volume 53 of *Texts in Applied Mathematics*. Springer, New York, 2008. Averaging and Homogenization.
- [40] R. Pinnau, C. Totzeck, O. Tse, and S. Martin. A consensus-based model for global optimization and its mean-field limit. *Math. Models Methods Appl. Sci.*, 27(1):183–204, 2017.
- [41] G.M. Rotskoff and E. Vanden-Eijnden. Neural Networks as Interacting Particle Systems: Asymptotic Convexity of the Loss Landscape and Universal Scaling of the Approximation Error. *arXiv:1805.00915*, 2018.
- [42] M. Shiino. Dynamical behavior of stochastic systems of infinitely many coupled nonlinear oscillators exhibiting phase transitions of mean-field type: H theorem on asymptotic approach to equilibrium and critical slowing down of order-parameter fluctuations. *Physical Review A*, 36(5):2393–2412, 1987.

- [43] J. Sirignano and K. Spiliopoulos. Mean Field Analysis of Neural Networks. *arXiv:1805.01053*, 2018.
- [44] Y. Tamura. On asymptotic behaviors of the solution of a non-linear diffusion equation. *J. Fac. Sci. Univ. Tokyo*, 31:195–221, 1984.
- [45] J. Tugaut. Phase transitions of McKean-Vlasov processes in double-wells landscape. *Stochastics*, 86(2):257–284, 2014.
- [46] C. Villani. *Topics in optimal transportation*, volume 58 of *Graduate Studies in Mathematics*. American Mathematical Society, Providence, RI, 2003.
- [47] P. Yatsyshin, N. Savva, and S. Kalliadasis. Spectral methods for the equations of classical density-functional theory: Relaxation dynamics of microscopic films. *J. Chem. Phys.*, 136:124113, 2012.
- [48] P. Yatsyshin, N. Savva, and S. Kalliadasis. Geometry-induced phase transition in fluids: Capillary prewetting. *Phys. Rev. E*, 87:020402(R), 2013.
- [49] P. Yatsyshin, A.O. Parry, and S. Kalliadasis. Complete prewetting. *J. Phys.: Condens. Matter*, 28:275001, 2016.
- [50] P. Yatsyshin, A.O. Parry, C. Rascón and S. Kalliadasis. Wetting of a plane with a narrow solvophobic stripe. *Mol. Phys.*, 116:1990-1997, 2018.
- [51] Z. Trstanova. *Mathematical and algorithmic analysis of modified Langevin dynamics*. PhD thesis, Université Grenoble Alpes, 2016.